



Article

Structural Mechanics of the Flight Feather Rachis: The Role of Cortical Keratin Asymmetry

Hao Wu 1,2,† , Ju-Cheng Hsiao 3,†, Wan-Chi Liao 3,4 , You-Sian Wang 4, Xiang-Ning Xie 3 and Wen-Tau Juan 3,5,*

- Graduate Institute of Biomedical Sciences, China Medical University, Taichung 404328, Taiwan; d109052001@mail.nchu.edu.tw
- ² Department of Life Sciences, National Chung Hsing University, Taichung 402202, Taiwan
- Department of Biomedical Imaging and Radiological Science, China Medical University, Taichung 404328, Taiwan
- Master Program for Biomedical Engineering, China Medical University, Taichung 404328, Taiwan
- Department of Medical Research, China Medical University Hospital, Taichung 404327, Taiwan
- * Correspondence: wtjuancmu@gmail.com
- [†] These authors contributed equally to this work.

Abstract: The flight feather rachis is a lightweight, anisotropic structure that must withstand asymmetric aerodynamic loads generated during flapping flight—particularly under unidirectional compression during the wing downstroke. To accommodate this spatiotemporal loading regime, the rachis exhibits refined internal organization, especially along the dorsoventral axis. In this study, we used finite element modeling (FEM) to investigate how dorsoventral polarization in cortical keratin allocation modulates the mechanical performance of shaft-like structures under bending. All models were constructed with conserved second moments of area and identical material properties to isolate the effects of spatial material placement. We found that dorsal-biased reinforcement delays yield onset, enhances strain dispersion, and promotes elastic recovery, while ventral polarization leads to premature strain localization and plastic deformation. These outcomes align with the dorsally thickened rachises observed in flight-specialized birds and reflect their adaptation to asymmetric aerodynamic forces. In addition, we conducted a conceptual exploration of radial (cortex-medulla) redistribution, suggesting that even inner-outer asymmetry may contribute to directional stiffness tuning. Together, our findings highlight how the flight feather rachis integrates cortical material asymmetry to meet directional mechanical demands, offering a symmetry-informed framework for understanding biological shaft performance.

Keywords: feather rachis; keratin polarization; finite element modeling; directional loading; anisotropic reinforcement



Academic Editor: Arkadiusz Chworos

Received: 19 April 2025 Revised: 30 May 2025 Accepted: 1 June 2025 Published: 5 June 2025

Citation: Wu, H.; Hsiao, J.-C.; Liao, W.-C.; Wang, Y.-S.; Xie, X.-N.; Juan, W.-T. Structural Mechanics of the Flight Feather Rachis: The Role of Cortical Keratin Asymmetry.

Symmetry 2025, 17, 880. https://doi.org/10.3390/sym17060880

Copyright: © 2025 by the authors. Licensee MDPI, Basel, Switzerland. This article is an open access article distributed under the terms and conditions of the Creative Commons Attribution (CC BY) license (https://creativecommons.org/licenses/by/4.0/).

1. Introduction

Biological materials often achieve remarkable functional performance, not through chemical diversity but through the spatial organization of compositionally simple building blocks. Studies have shown that natural structural materials gain exceptional strength and toughness through hierarchical architectures and functional synergy, even when composed of simple components [1,2]. The hierarchical design of biological composites—such as wood, bone, and nacre—enables them to exhibit outstanding mechanical performance for multifunctional applications [3,4]. Among these biological composites and polymers, keratin stands out for its exceptional versatility, displaying superior mechanical, thermal, and optical properties, making it a valuable model for bioinspired designs [5,6].

Symmetry 2025, 17, 880 2 of 17

Unlike engineered systems that rely on a wide array of specialized materials, living organisms frequently repurpose a limited set of molecular components into structurally diverse and functionally adapted forms. For example, collagen in the musculoskeletal system supports both tensile tendons and rigid bone [3], while keratin in skin and its appendages gives rise to soft epidermis, rigid scales, flexible claws, and load-bearing feathers [5,7,8]. The role of keratin in skin regeneration—particularly its expression during wound healing—further underscores its importance in maintaining the structural and functional integrity of skin appendages [9]. This capacity to generate functional diversity from a conserved molecular toolkit highlights the significance of spatial organization and symmetry-related design principles in biological materials.

Among keratin-based structures, the avian feather rachis stands out as a lightweight, anisotropic, and resilient shaft capable of withstanding repetitive aerodynamic loads. With its high specific strength and structural economy, the rachis has attracted interest as a model in both biomechanics and biomimetic materials research. Its compositionally simple yet hierarchically integrated architecture has been the subject of intensive empirical work [4,10–22], highlighting how keratin organization contributes to remarkable energy absorption, flexural stiffness, and direction-dependent stability. The rachis achieves its mechanical robustness through a hierarchical design, where complex arrangements of keratin fibers and elements across scales provide an optimized balance of strength, flexibility, and lightweight performance [10,12,13]. Species-specific adaptations further enhance these properties, with variations in laminar composition, cross-sectional geometry, and fiber orientation optimizing mechanical performance for different flight styles [11,16–19]. The mechanical anisotropy, driven by the hierarchical organization of keratin fibers, governs tensile strength, fracture behavior, and load distribution [20,21]. Recent autofluorescence microscopy revealed how keratin density and assembly influence regional mechanical strength along with branching feather growth [14,19–21]. In the rachis core, the presence of foam-filled medullary regions provides damping properties that improve energy absorption and vibration control, maintaining flight stability even under dynamic loading [22]. This combination of hierarchical design, species-specific adaptation, anisotropic behavior, and damping capacity makes the feather rachis an exceptional example of nature's ability to achieve mechanical efficiency through spatial organization rather than material complexity.

This asymmetry-driven mechanical performance has motivated a range of studies aimed at characterizing keratin integration in the rachis cortex. Traditional material tests have reported bulk stiffness and flexural properties along the rachis [16,17,19–22]. However, while several studies have noted cross-sectional asymmetries in feather rachises [13,16,19,20,23], systematic investigation of these features—particularly along the dorsal-ventral (D-V) and lateral axes—remains limited. To resolve these subtleties, we previously developed a morphometric pipeline to quantitatively analyze rachis crosssections [13,24]. Applying this to multiple avian lineages [13,25], we revealed that flightspecialized birds tend to exhibit subtle but consistent D-V polarization of cortical geometry. More recently, we used autofluorescence microscopy to map keratin density distributions with high spatial fidelity [14], showing that mechanical heterogeneity is shaped not only by morphology but also by regional material content—further supporting the presence of spatially patterned keratin allocation within the cortex. These findings suggest that keratin polarization—in both geometric and compositional terms—plays a role in tailoring the rachis to species-specific flight demands. However, while the anatomical and developmental basis of these patterns is increasingly well-characterized [13,25], their mechanical consequences remain less well understood. In particular, it is unclear how variations in material distribution across the cortex affect local stress routing, strain accumulation, and overall shaft performance. The lack of studies directly addressing this gap limits our

Symmetry 2025, 17, 880 3 of 17

ability to interpret morphological adaptations in mechanical terms or to translate these symmetry-informed design principles into engineered structures.

To address this gap, we applied finite element modeling (FEM) to test how D–V asymmetry in cortex allocation influences mechanical behavior under bending. FEM has become a widely adopted tool in the study of avian feather rachises, enabling researchers to simulate and analyze their complex mechanical behaviors under various loading conditions [16–22]. Rather than reproducing the full morphological variety observed across birds, we focused on square and rectangular cross-sections—an empirically supported shaft shape among flight-specialized birds [13,19,23]—to isolate the role of material placement. This modeling framework was selected to capture broadly applicable biomechanical principles, allowing for the isolation of geometric effects without confounding influences from species-specific shape variation.

In this study, the emphasis is on how the spatial distribution of a single material—rather than its composition—determines mechanical performance. Our FEM approach standardizes material properties across all models, ensuring that observed differences arise solely from spatial variation. This approach highlights a core principle in biological design: optimization often emerges from the strategic spatial placement of simple materials rather than from the use of complex or exotic substances. We aim to demonstrate that, even with identical material properties, dorsal reinforcement significantly improves strain distribution, delays yield onset, and enhances elastic recovery—indicating that spatial asymmetry contributes substantially to mechanical performance, even when compositional variation is absent. While simplified, this approach allows for us to disentangle the effects of keratin distribution from those of shape-related mechanics, providing a controlled framework to evaluate how spatial asymmetry modulates strain dynamics, yield onset, and post-deformation recovery. This strategy is supported by our recent biological findings in frizzling feathers, where dorsoventral disruption in cortex development led to mechanical dysfunction, illustrating the role of spatial material asymmetry in rachis performance [26], as further discussed in the Discussion section. The feather rachis thus provides a compelling example of how functionally adaptive mechanics can emerge from compositionally simple but spatially asymmetric architectures—offering insight into the broader relationship between structural asymmetry and mechanical function in natural systems.

2. Materials and Methods

2.1. Model Construction and Geometric Framework

To evaluate the mechanical effects of symmetry breaking via dorsoventral (D–V) keratin distribution in the feather rachis cross-section, a series of simplified two-dimensional finite element models were constructed. Each model was composed of four rectangular cortical blocks—dorsal, ventral, and two lateral segments—assembled into a hollow square or rectangular tube to simulate a feather shaft cross-section. This modular design mimics the typical organization of the cortex in flight feather rachises, allowing for precise geometric control over both baseline symmetry and directional asymmetry while maintaining generalizability and minimizing confounding effects from species-specific shape differences.

To account for natural variation in rachis size across bird species, all models were scaled relative to the cortex-to-total cross-sectional area ratio measured in the duck feather shaft (*Anas platyrhynchos domesticus*). The baseline model featured a geometrically symmetric square cross-section with a side length of 16.23 mm, approximately 10 times the actual width of a duck feather shaft at the mid-proximal region. The cortical shell occupied 27.9% of the total cross-sectional area. The overall shaft length was set to 120 mm, with a 100 mm span between the two supports in the three-point bending setup, ensuring consistent aspect

Symmetry 2025, 17, 880 4 of 17

ratios across all simulations. Geometries were created in SolidWorks (v2014) and exported as Parasolid (x_b) files to ANSYS Workbench (R17.2) for further analysis.

Each model was discretized using hexahedron elements, appropriate for simulating mid-span deformation in long beams. The average element size was approximately $0.4 \, \mathrm{mm}$, with a total of $\sim 160,000-185,000$ elements, depending on model geometry. Mesh sensitivity analysis was conducted to ensure that the stress and displacement results were independent of mesh density, with convergence defined as a change of less than 1% in maximum stress values between successive mesh refinements. To conserve simulation resources, the presented results were generated without element refinement near interfaces and curved regions. This decision followed a thorough evaluation confirming that the accuracy and consistency of key reported features were not significantly affected by the absence of local refinement.

2.2. Material Properties and Assignment Strategy

All simulations employed the same material definition across all regions of the cortex to isolate the effects of geometry-induced symmetry variation. Each model used a bilinear elastic–plastic material model. Young's modulus was set to 5 GPa, representing the material property of feather rachis keratin, which typically ranges from 3 to 7 GPa [16,19]. Poisson's ratio was fixed at 0.3, a commonly used value for keratinous materials [19,23]. The yield strength—defined as the onset of bilinear isotropic hardening in ANSYS—was set to 138 MPa, based on prior experimental data reporting the tensile strength of keratin fibers reconstituted from feather shafts [27]. Beyond yield, the material response was modeled as perfectly plastic, with a tangent modulus of 50 MPa, consistent with the brittle behavior of keratin materials [5].

This uniform material assignment ensured that all observed differences in mechanical response among model variants were attributed solely to geometry-based symmetry breaking—including the spatial distribution and relative thickness of cortex regions—rather than to differences in intrinsic material properties.

2.3. Medulla Exclusion and Geometric Justification

The medullary core of the rachis was excluded from all models. This decision was based on prior empirical observations showing that the medulla exhibits a porous, foam-like morphology and has significantly lower stiffness than the surrounding cortex—by orders of magnitude—and, therefore, contributes minimally to the shaft's bending resistance [21,28]. By excluding the medulla, we focused computational resources on the cortical shell, which dominates load-bearing mechanics and asymmetry-driven strain distribution under bending conditions.

2.4. Boundary Conditions and Loading Scheme

All simulations were conducted under quasi-static, three-point bending conditions using ANSYS's static structural solver. The shaft was supported laterally by two 2 mm-wide virtual contact plates positioned symmetrically 100 mm apart. These supports constrained vertical motion but allowed for longitudinal sliding to avoid reaction force artifacts. A rigid structural-steel cylindrical indenter (6 mm radius, 24 mm length) was used to apply vertical displacement at the dorsal midline of the shaft, simulating the compressive load experienced during the downstroke phase of flapping flight. The displacement ranged from 0 to 5 mm. The finite contact area of the indenter minimized stress concentration effects and ensured stable convergence during loading.

The simulations assumed plane-strain conditions and were run with enabled large deformation settings to accommodate geometric nonlinearities where applicable. Output variables included equivalent von Mises stress, total strain, and overall deformation pro-

Symmetry 2025, 17, 880 5 of 17

file. Key structural performance indicators were extracted at three displacement stages: pre-yield, yield onset, and post-yield plateau. This symmetrically controlled loading setup provided a consistent baseline for evaluating how dorsoventral asymmetry in cortex structure influences mechanical outcomes.

2.5. Model Variants and Comparative Design

Two classes of models were constructed for comparative analysis:

- Symmetric baseline model: A square cross-section with uniform cortex thickness and consistent material properties on all four walls.
- Asymmetric D–V model: Variants with cortex geometries modified based on dorsoventral thickening patterns observed in prior morphometric analyses of avian feather shafts [13,25].

All models shared identical material parameters, meshing resolution, and boundary conditions. Comparative metrics included effective stiffness, yield displacement, strain localization, and plastic deformation recovery. This contrast between geometrically symmetric and biologically informed asymmetric configurations enabled a targeted investigation of symmetry breaking in structural performance. Our models isolate the mechanical effects of dorsoventral (D–V) polarization while intentionally excluding factors such as medullary porosity, laminar microstructure, and dynamic loading to maintain computational efficiency.

A key design constraint was the conservation of the second moment of area (I), which governs bending resistance. By keeping I constant across all configurations and varying only the spatial distribution of cortical material, we ensured that differences in mechanical response arose purely from internal asymmetry rather than global stiffness. This design reflects the biological principle that keratin allocation can be spatially optimized without altering overall shaft geometry.

2.6. Compressive Testing of Real Feather Rachises

To support our FEM-based findings, we performed simplified compressive tests on proximal rachis segments (~2 cm in length and ~2 mm in thickness) from adult chicken and duck feathers. Each specimen was tested along three directions—dorsal (D), ventral (V), and lateral (L)—using a flat steel probe mounted on a vertical depth gauge. Compressive modulus was estimated by normalizing the indentation depth to local rachis thickness. Measurements were repeated five times at three locations per direction and averaged. Statistical comparisons were performed using two-tailed *t*-tests. The results are shown in Figure 1C.

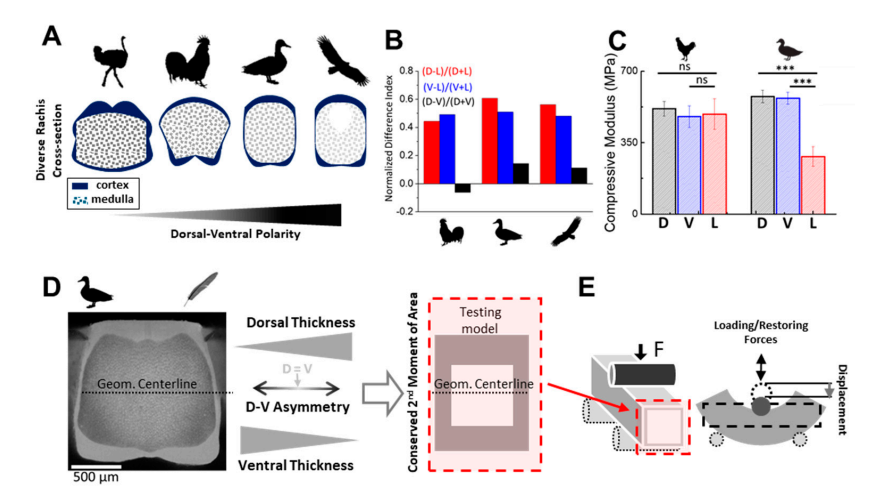


Figure 1. Modular abstraction of rachis cortical architecture for finite element simulation. (A) Cross-species schematic of dorsal-ventral cortex variation in nature based on the discovery of ref. [13]. (B) The

Symmetry **2025**, 17, 880 6 of 17

normalized difference index of the mean normalized cortex thickness (mean NCT) of the dorsal (D), ventral (V), and lateral (L) cortex of flight feather rachis of the chicken, duck, and eagle. Raw data were extracted from ref. [13] to quantify D–V and lateral asymmetry in cortical thickness. (C) Compressive modulus (MPa) of primary feather rachises from chicken and duck, measured along the dorsal (D), ventral (V), and lateral (L) directions. Within-species comparisons among the three directions were analyzed using one-way ANOVA, followed by post hoc tests. Between-species comparisons for each direction were assessed using two-tailed t-tests. "ns" indicates non-significant differences (p > 0.05). *** indicates p < 0.001. Error bars represent the standard deviation across repeated tests for each condition. (D) Representative autofluorescence image of a duck flight feather rachis cross-section, showing dorsoventral asymmetry in cortex thickness. Dorsal and ventral cortex regions were separately defined and systematically varied in thickness to generate testing model configurations under conservation of the second moment of area (I) relative to the geometrical centerline. (E) Schematic of the three-point bending simulation: fixed lateral supports, dorsally applied displacement, and output metrics include equivalent von Mises stress, total strain, and overall deformation profile.

3. Results

3.1. From Biological Variation to Finite Element Modeling: A Modular Cortical Framework

The avian feather rachis exhibits substantial morphological variation across species, particularly in the organization of its cortical shell. In our previous comparative work [13], we showed that differences in dorsal, ventral, and lateral cortex thickness correspond to distinct flight adaptations, influencing how the shaft resists bending and torsion (Figure 1A). The geometric polarity along the dorsal–ventral axis of the mid-proximal rachis cross-sections among chicken, duck, and eagle flight feathers was evidenced by the normalized difference index of the mean normalized cortex thickness (mean NCT) from [13], as shown in Figure 1B.

Furthermore, compressive tests conducted on real flight feather rachises of chicken and duck (Figure 1C) revealed notable species-specific differences in mechanical behavior. Duck rachises, which exhibit pronounced dorsoventral cortical polarization, showed significantly higher compressive stiffness along the D–V axis compared to the lateral axis. In contrast, chicken rachises, showing less dorsoventral polarity and more prominent lateral features, displayed a nearly isotropic stiffness profile. These findings reinforce the hypothesis that D–V geometrical polarization enhances directional stiffness and structural performance, providing empirical support for the modeling assumptions adopted in this study. To translate these biological observations into a computational framework, we abstracted high-resolution autofluorescence images [14] into simplified cortex profiles suitable for finite element modeling, as demonstrated in Figure 1D.

We approached the rachis cortex as a modular structure comprising dorsal (D) and ventral (V) segments, with geometric variability captured through systematic combinations of wall thickness profiles (Figure 1D). This approach reflects the empirical observation that D and V regions vary semi-independently across species and allows for us to isolate the influence of dorsoventral symmetry breaking under controlled mechanical settings.

All model configurations preserved the I relative to the rachis geometrical centerline and used identical material properties, ensuring that observed differences in performance arose solely from geometry-induced asymmetry. Each D/V pair was assembled into a square or rectangular cross-section and subjected to three-point bending simulation (Figure 1D,E), enabling us to test how structural asymmetry governs deformation behavior. Although the models are abstracted from biological morphotypes, they retain the core mechanical logic observed in rachis design. The following sections examine whether such minimal geometric differences can lead to notable changes in mechanical behavior and strain distribution.

Symmetry **2025**, 17, 880 7 of 17

3.2. Dorsoventral Cortex Polarization Modulates Bending Strength and Strain Localization

To evaluate the structural consequences of dorsoventral (D–V) asymmetry, we simulated four configurations of square-tube cortex models, all constructed with identical material properties and a conserved *I*: a fully symmetric model, a bi-polarized model with balanced dorsal and ventral thickening, a dorsal-polarized model, and a ventral-polarized model (Figure 2A). All configurations were subjected to the same three-point bending conditions to isolate the effects of geometric redistribution.

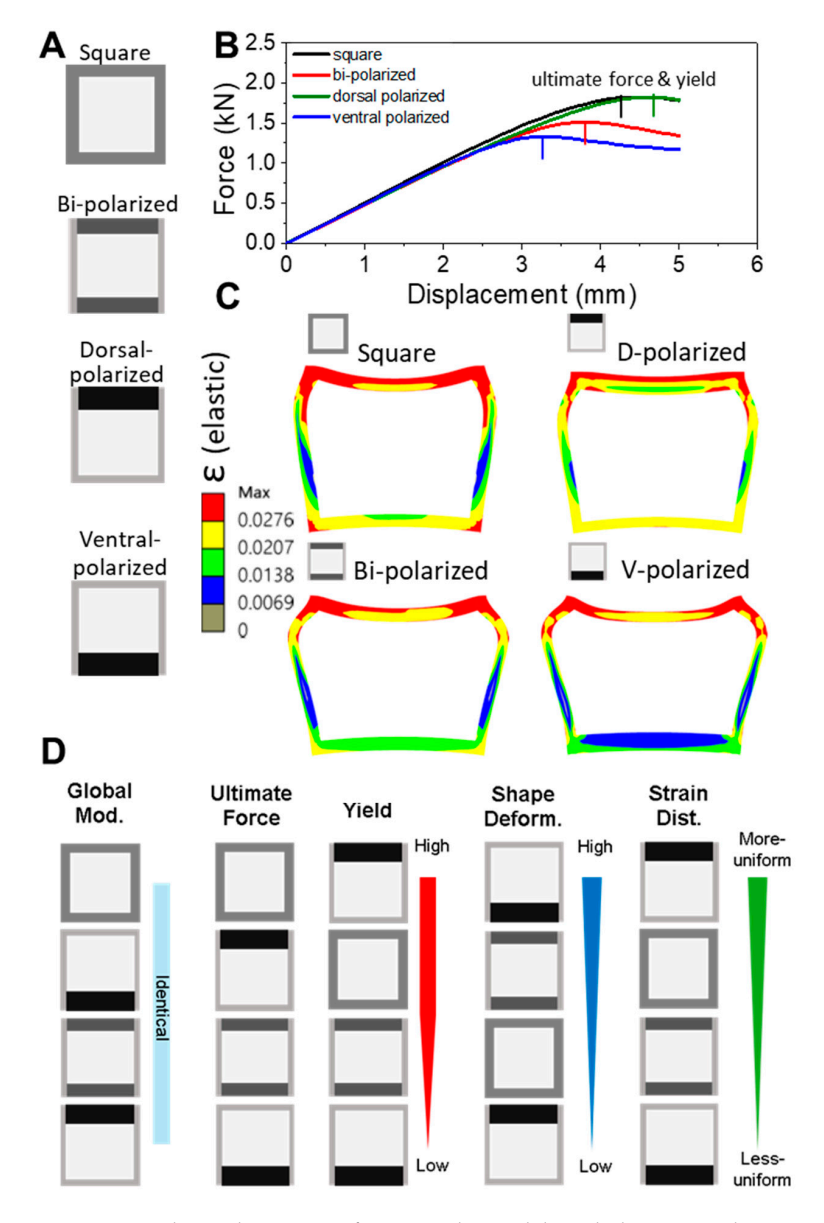


Figure 2. Mechanical response of square-tube models with dorsoventral cortex asymmetry. (**A**) Schematics of four modeled configurations with identical I: symmetric, bi-polarized, dorsal-polarized, and ventral-polarized cortex distributions. (**B**) Force–displacement curves under three-point bending, obtained through finite element simulation (FEM). Colored vertical lines represent the ultimate force and yield points corresponding to each curve. Dorsal-polarized models show delayed yield and high force capacity; ventral-polarized fail early. (**C**) Strain maps (maximum total strain, ε) at equivalent displacement stages. Dorsal- and bi-polarized models show broader strain distribution, while ventral-polarized models exhibit significant dorsal-lateral concentration. (**D**) Summary metrics of model performance across stiffness, yield behavior, and strain uniformity. Dorsal-polarized configuration ranks highest in strain uniformity and mechanical resilience, highlighting the effect of cortex geometry alone.

Symmetry 2025, 17, 880 8 of 17

The resulting force–displacement curves (Figure 2B) revealed that both the dorsal-polarized and symmetric bi-polarized models achieved similarly high ultimate force, but the dorsal-polarized configuration sustained greater displacement before yielding. In contrast, the ventral-polarized model exhibited the lowest load-bearing capacity and the earliest yield, while the bi-polarized model showed intermediate performance. This demonstrates that dorsal reinforcement delays the onset of plastic deformation, as indicated by the right-shifted inflection point in the force–displacement curve. These findings suggest that dorsal-side reinforcement offers a mechanical advantage under compressive dorsal loading, such as that experienced during the downstroke phase of wing flapping.

Strain maps visualized at equivalent displacement stages (Figure 2C) illustrate how cortical asymmetry affects deformation pathways. The dorsal- and bi-polarized models exhibited diffuse and uniform strain dispersion across the dorsal-ventral arcs and lateral sides. In contrast, the ventral-polarized model developed highly concentrated strain zones near the dorsal midline and upper lateral cortex patterns associated with premature local failure. A comparative summary of key mechanical metrics is presented in Figure 2D, including effective modulus, ultimate force, yield displacement, and strain distribution quality. The dorsal-polarized models consistently scored highest in both resilience and strain moderation, whereas the ventral-polarized models performed poorest across these criteria. Importantly, these differences arose despite conserved material properties and global stiffness, reinforcing that cortical geometry alone governs critical performance outcomes. The close correspondence between early yield and localized strain accumulation suggests a fundamental link between spatial material asymmetry and strain localization—a concept further examined in Section 3.3.

3.3. Strain Population and Spatial Mapping Reveal Propagation Patterns and Weak Points

To further understand the deformation dynamics underlying cortical asymmetry, we analyzed the internal strain behavior of the bi-polarized (dorsal-ventral symmetrically thickened) model as a representative case. This configuration showed intermediate performance in the force-displacement response obtained through finite element simulation (Figure 2B), and we used it to explore how strain population characteristics translate into spatial mechanical behavior under load.

Strain population histograms (Figure 3A) showed that the bi-polarized and symmetric models maintained moderately concentrated strain profiles, both with distinct peaks around 0.009–0.010 strain units and extended tails into higher strain ranges. Compared to the dorsal-polarized configurations—where considerable elements clustered in a narrow strain band around 0.011—the bi-polarized and symmetric models displayed a broader distribution, suggesting uneven engagement of material. In contrast, the ventral-polarized configuration produced flatter, more skewed distributions dominated by low-strain zones and scattered strain hotspots. This strain histogram profile reflects poor cortical engagement and suggests enhanced localization within confined strain zones—consistent with the abrupt failure seen in this configuration.

To interpret the structural implications of this population profile, we mapped the spatial strain behavior of the bi-polarized model under loading at a displacement of 4.52 mm. In the cross-sectional view (Figure 3B), a concentration zone emerged near the dorsal midline—aligned with the site of load application—indicating early-stage strain localization. The 3D volume rendering (Figure 3C) confirmed that strain accumulation propagated both longitudinally and radially within a localized region centered around the dorsal and upper lateral cortex in the loading zone, while the ventral and lower lateral regions remained largely underutilized.

Symmetry 2025, 17, 880 9 of 17

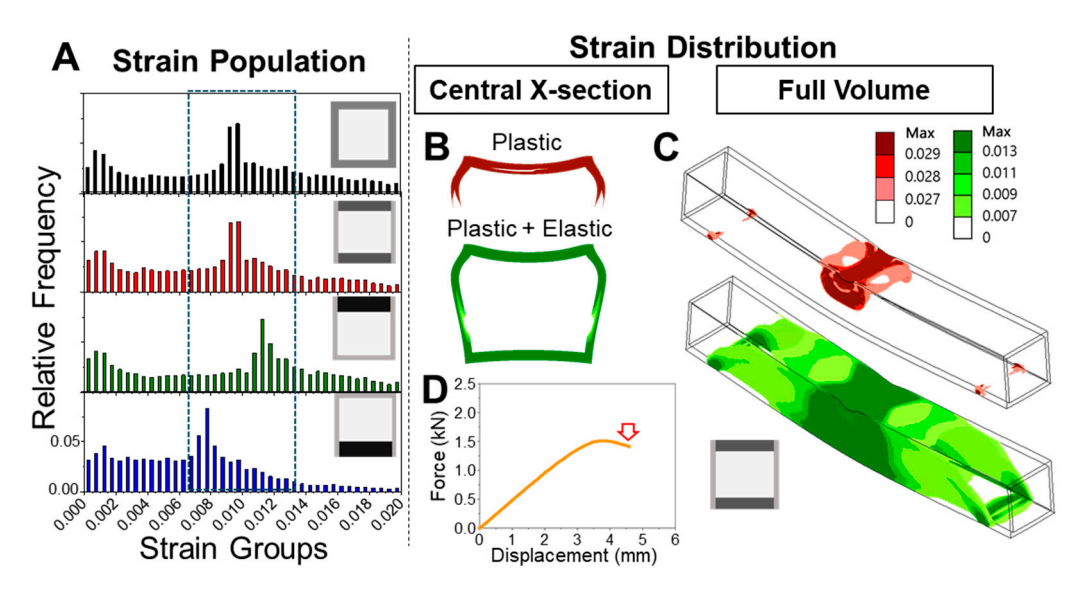


Figure 3. Strain distribution and plastic onset illustrated in the bi-polarized cortex model. (**A**) Strain population histogram for all four cortex models near the plastic transition. Dashed boxes highlight the strain ranges most densely populated in each configuration. The bi-polarized model was selected as a representative case to explore the implications of strain distribution profiles in (**B–D**). (**B**) Cross-sectional strain map of the central plane shows localized strain localization near the dorsal midline around the loading site. (**C**) Three-dimensional (3D) strain rendering reveals that this dorsal hotspot propagates longitudinally within a confined corridor, while other regions remain relatively unengaged. (**D**) Force–displacement curve for the same model, with the plastic transition (~4.52 mm, indicated by arrow) corresponding to the onset of localized strain build-up in (**B**,**C**).

Importantly, this localized strain build-up corresponded to the onset of nonlinearity in the force–displacement curve (Figure 3D), deviating from linearity near 3.5 mm displacement—signaling the global transition from elastic to plastic behavior. Despite constant global geometry and material properties across models, these results show that strain localization alone—governed by cortex geometry—can drive premature yielding.

While our models are abstracted, the dorsal-side strain localization is noteworthy, as similar regions are implicated in experimental failure patterns under dorsal-side compression during mechanical testing of feather shafts in our recent experiment (see Section 4, Discussion for details). Although in vivo validation remains limited, our findings illustrate how structural reinforcement strategies, even when symmetric, can lead to localized mechanical vulnerability under directional loads.

3.4. Yield Initiation Progression Reveals Spatial and Temporal Deformation Dynamics

To understand how different dorsoventral (D–V) cortex configurations influence the timing and spatial sequence of yielding, we analyzed the force–displacement behavior of each model alongside its internal deformation patterns. Building on the local strain dynamics observed in Figure 3, we now focus on how and when the transition from elastic to plastic behavior occurs and how this process varies across geometrically distinct configurations.

Figure 4A presents a schematic summary of three distinct deformation stages that universally occur during bending, though at different displacement thresholds depending on cortex geometry, where the red zone indicates the strain hotspot:

• Stage I (Light-blue frame): At low applied force, all models exhibit broadly distributed deformation with minimal strain localization. The tube retains its square form, and behavior remains largely elastic.

Symmetry 2025, 17, 880 10 of 17

• Stage II (Green frame): Strain propagation reaches the upper lateral cortices, forming localized deformation zones near the dorsal corners. This marks the transition phase and the onset of plastic-dominated response.

 Stage III (Black frame): With continued loading, strain concentrates along the dorsal midline beneath the loading point. This stage marks asymmetric strain localization and regional softening, ultimately leading to failure.

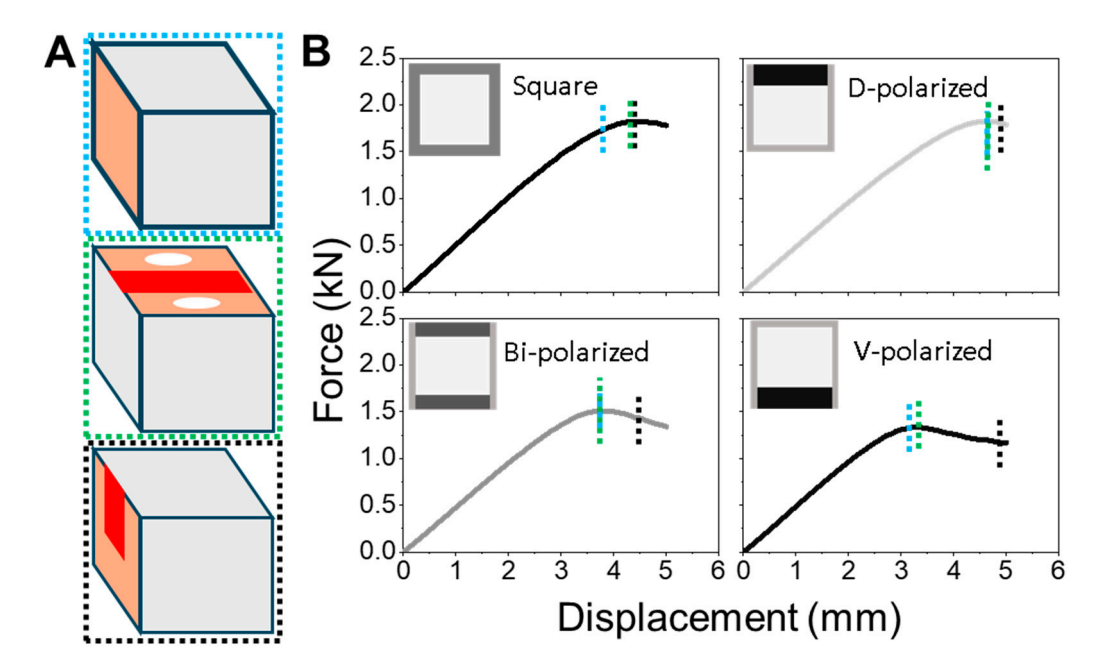


Figure 4. Temporal progression of strain localization and its relation to mechanical yield across D–V cortex configurations. (A) Schematic depiction of three universal deformation stages. Light-blue: Early distributed elastic deformation, square shape retained. Green: Lateral strain zones appear, marking the transition to plastic deformation. Black: Dorsal midline strain localization emerges beneath the loading point, initiating asymmetric strain localization. Red regions indicate areas of high strain concentration, while the orange region indicates areas of lower strain distribution during deformation. (B) Force–displacement curves for square, dorsal-, bi-, and ventral-polarized models. Colored dashed lines indicate the displacement at which each deformation stage transitions. Blue: End of elastic regime. Green: Onset of lateral strain and plastic behavior. Black: Peak dorsal strain localization. The bi-polarized model in the bottom-left panel is the same simulation analyzed in Figure 3B–D, linking localized strain development with macroscopic yield behavior and revealing how symmetry-breaking geometry governs performance.

These three stages are temporally mapped in Figure 4B for each configuration. The light-blue, green, and black dashed lines indicate the displacements marking the end of Stage I (elastic deformation), the transition between Stages II and III (strain redistribution), and the onset of plastic deformation, respectively. The relative spacing and order of these thresholds differ between models, reflecting variation in strain tolerance and yield progression.

For example, the square and dorsal-polarized models (upper panels in Figure 4B) delay the emergence of localized strain, reaching the green threshold at higher displacements. This indicates more gradual and controlled yielding behavior. In contrast, the ventral-polarized model enters plasticity early, with rapid development of lateral strain zones. The bi-polarized model falls between these extremes, showing clear staging but reduced displacement tolerance.

Notably, the bi-polarized configuration in Figure 4B corresponds to the same model analyzed in Figure 3B–D. This directly links spatial strain maps (2D and 3D) with global

Symmetry 2025, 17, 880 11 of 17

force–displacement behavior, revealing how regional strain build-up precedes yield at the structural level.

Together, these findings demonstrate that the sequence and timing of regional strain localization—driven by symmetry-breaking geometry—govern mechanical resilience. Reinforcement strategies such as dorsal polarization extend the elastic regime and delay instability, whereas ventral asymmetry accelerates failure. Understanding these spatial-temporal dynamics provides deeper insight into the design logic of feather shafts and other asymmetrically reinforced, hollow biological beams.

3.5. Strain Localization and Recovery Dynamics in Polarized Cortical Architectures

To further dissect the failure mechanisms introduced in Section 3.4, we extended the analysis of the ventral-polarized configuration—identified as the structurally weakest design in terms of early strain localization and plastic onset. While the models share comparable global shape and bending moment, the internal strain localization diverges substantially due to asymmetries in cortical geometry and material distribution.

Figure 5A presents sequential strain maps from the ventral-polarized model—which exhibited the lowest yield capacity among all configurations—capturing three key displacement stages (d_{yield} , d_{middle} , d_{end}). These snapshots illustrate that, once dorsal strain localization emerges, the strain zones remain spatially fixed and resist redistribution, especially into the ventral cortex. Because strain cannot redistribute effectively, deformation becomes confined to a small region of the shaft and persists throughout loading—this localized weakness ultimately governs the mechanical response of the entire structure. These features extend the temporal yield progression discussed in Figure 4 and provide spatial context for the early failure of ventral-polarized models under asymmetric loading.

To evaluate post-yield behavior, we simulated a full loading–unloading cycle for the same configuration (Figure 5B). Strain mapping revealed that deformation remained concentrated along the dorsal midline and upper lateral cortex, even after unloading. The presence of residual strain indicates widespread plastic deformation, not only in initially overburdened regions but also extending into adjacent zones, including the ventral cortex. This suggests that, once yielding begins, it cascades across a large fraction of the cortex due to ineffective strain redistribution. The corresponding force–displacement curve exhibits a pronounced hysteresis loop, as shown in the right panel, confirming substantial energy loss and limited elastic recovery. Together, these observations point to the mechanical liabilities introduced by lower-side reinforcement: localized strain focusing, redistribution failure, and irreversible deformation.

Finally, Figure 5C places these findings in the context of broader keratin allocation strategies discovered in earlier work [13]. While our primary models focused on dorsoventral cortical polarization, biological feather shafts also exhibit variation in radial symmetry—specifically, in the relative allocation of keratin between the cortex and medulla. In these conceptual simulations, we tested how material redistribution affects bending and compression stiffness under volume-conserving assumptions. In the left panel, cortex polarization (i.e., increasing lateral asymmetry) results in reduced bending stiffness but increased compressive resistance, mimicking patterns found in functional shaft zones. In the right panel, medulla depletion—which represents a shift toward denser cortex walls, usually found in feathers of birds with sustained or powered flight—yields a gain in both bending and compressive stiffness. These results suggest that the medulla may serve as a tunable material reservoir, allowing for shafts to balance mechanical demands through both internal (radial) and external (D–V) polarization. While these effects lie beyond the scope of our primary simulations, they offer a conceptual bridge for future work on generalized symmetry-breaking strategies in feather shaft design.

Symmetry **2025**, 17, 880 12 of 17

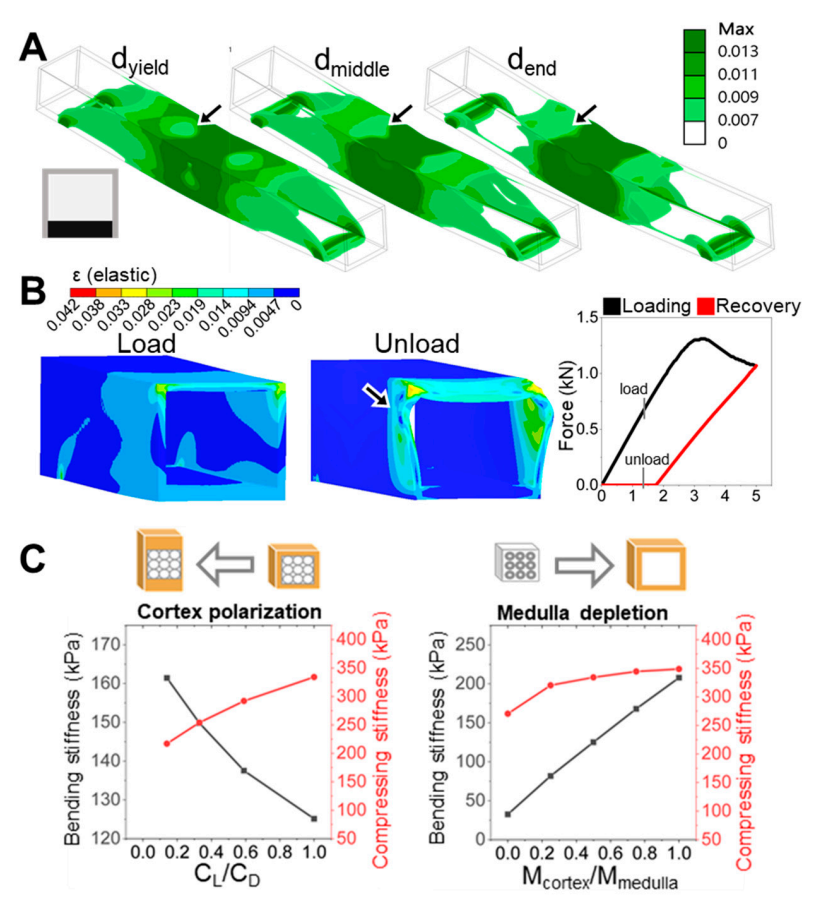


Figure 5. Propagation, recovery, and polarization effects in asymmetric cortex models. (**A**) Sequential elastic strain maps from the ventral-polarized configuration at three displacements: d_{yield} , d_{middle} , and d_{end} . Black arrows indicate strain zones that appear early and remain spatially isolated despite continued loading. This rigidity in strain propagation restricts redistribution and contributes to asymmetric failure behavior. (**B**) (**Left**) Strain mapping before and after a full loading–unloading cycle reveals plastic deformation (indicated by black arrow) retained along the dorsal midline and upper lateral cortex. (**Right**) The force–displacement curve shows a pronounced hysteresis loop, indicating poor recoverability and significant energy loss. (**C**) Conceptual simulations comparing two polarization strategies under keratin volume conservation. (**Left**) D–V polarization increases compressive stiffness but compromises bending resistance. (**Right**) Medulla depletion—representing radial symmetry breaking—enhances both bending and compressive stiffness, highlighting the medulla's potential role as a tunable keratin reservoir in structural optimization.

4. Discussion

This study demonstrates that even modest shifts in cortical keratin distribution can significantly influence the mechanical performance of hollow biological beams such as feather shafts. By manipulating dorsoventral (D–V) polarization in simplified square cross-sections, we show that dorsal-biased reinforcement improves resistance to bending, delays yield onset, and promotes more uniform strain distribution. In contrast, ventral polarization compromises these features, resulting in early strain localization, plasticity-dominated deformation, and poor structural recovery.

Our findings demonstrate that dorsal reinforcement delays strain localization, promotes elastic recovery, and aligns with natural adaptations in flight feather rachises. This pattern reflects the adaptive strategy of the thickened dorsal cortex in birds, optimizing mechanical resilience under asymmetric aerodynamic loading. These results underscore the role of spatial asymmetry—not simply material composition—in governing performance, even when volume and stiffness are globally conserved.

Symmetry 2025, 17, 880 13 of 17

Central to our modeling framework is the conservation of *I*, a geometric property that governs resistance to bending about a given axis. All FEM variants in this study were designed to maintain the same *I*, ensuring that differences in performance arose solely from spatial redistribution of cortical material—not from changes in global stiffness. By repositioning material dorsally or ventrally while preserving external dimensions, we could isolate how internal asymmetry affects strain behavior and mechanical resilience. This design principle reflects a biologically inspired strategy, where directional mechanical performance is tuned without significantly altering bulk shape or composition.

The superior performance of the dorsal-polarized models is tightly linked to the dominant mechanical environment of the feather rachis during flight. In the downstroke phase of flapping—a key moment for lift generation—the shaft bends upward, placing the dorsal cortex in compression and the ventral cortex in tension. Our FEM simulations reproduce this regime by applying displacement to the dorsal surface, effectively mimicking this loading condition. Reinforcing the dorsal side thus aligns with the aerodynamic stress pattern, providing targeted resistance where strain accumulates most. Additionally, the feather vane is anchored dorso-laterally, transmitting aerodynamic loads directly into the dorsal cortex. This anatomical configuration further concentrates mechanical demand on the dorsal surface, reinforcing the structural logic behind dorsal-side thickening in flight feathers.

In contrast, a ventral-thickened rachis would misalign with the dominant aerodynamic loading pattern, placing the dorsal side at risk of early strain localization and mechanical failure. Our simulations (Figure 5A,B) confirm that ventral reinforcement accelerates strain localization and yield onset, undermining structural resilience. Notably, such ventral-thickened rachises are more common in flightless birds like ostriches, where reduced flight demands relax the need for directional mechanical optimization [13]. This evolutionary comparison highlights that D–V polarization is an adaptive trait, providing load-specific mechanical optimization for active fliers.

These insights align with comparative morphological studies of flight feathers, where dorsal cortical thickening is a recurring pattern in birds exposed to high bending loads [13]. Our modeling results provide a structural and mechanical rationale for this evolutionary trend: asymmetric material placement—especially in the dorsal–ventral direction—emerges as an efficient strategy for tuning local stiffness and failure tolerance under directional aerodynamic loading. In this way, biological shafts such as the feather rachis demonstrate how internal symmetry breaking at the material level can yield adaptive advantages at the structural scale.

The alignment between our FEM simulation results and experimental measurements (Figure 1C) supports the central hypothesis that spatial redistribution of cortical material—while conserving *I* with similar volume—governs the directional mechanical performance of the feather rachis. Specifically, the higher stiffness along the D–V axis observed in duck rachises with dorsoventral cortical polarization, compared to the nearisotropic stiffness in chicken rachises with symmetric geometry, underscores the critical role of D–V asymmetry in enhancing directional stiffness and mechanical resilience.

The progression of strain localization in each model further clarifies how these shaft architectures either fail or resist failure. Using the ventral-polarized configuration as an example, strain zones initially concentrate near the dorsal midline and then extend laterally and even ventrally under continued displacement. These zones emerge early, remain spatially fixed (Figure 5A), and persist throughout the deformation cycle. Simulation of a full loading–unloading cycle revealed significant residual deformation (Figure 5B), consistent with a broad population of plastic elements and confirmed by a pronounced hysteresis loop in the force–displacement curve. These effects highlight a cascade mecha-

Symmetry 2025, 17, 880 14 of 17

nism: initial strain localization impedes redistribution, amplifying deformation and energy loss. In contrast, the dorsal-polarized models distribute strain more broadly and recover more elastically, suggesting a more resilient and dissipative deformation pathway. The ability—or failure—to redirect strain appears to be a critical determinant of post-yield mechanical behavior.

In this work, we focused on square and rectangular cross-sections—shapes frequently observed in the rachis of strong flyers [13]—to isolate the role of dorsoventral material asymmetry while minimizing confounding effects from geometry. This simplification allowed for us to decouple keratin distribution from shape-driven influences, such as dorsal curvature or moment-arm variation. While real feather shafts display more elaborate cross-sectional profiles (Figure 1), incorporating such complexity may obscure the effects of internal symmetry breaking. Nonetheless, features such as dorsoventral curvature or lateral ridges may further modulate strain pathways, potentially redistributing stress and delaying local failure. Given the asymmetrical aerodynamic forces during flapping, structural symmetry is not always mechanically optimal. Future studies integrating morphotype-specific geometry with material asymmetry may better resolve how natural shafts achieve performance tuning through multiscale symmetry modulation.

To conceptually extend our findings beyond dorsoventral (D–V) polarization, we explored an orthogonal form of symmetry breaking: radial material redistribution between the cortex and medulla. While structurally weaker, the medulla functions as a potential keratin reservoir that can be reallocated to reinforce specific regions of the shaft. Our FEM simulations showed that cortex-biased redistribution—effectively representing medulla depletion—increases both bending and compressive stiffness. In contrast, D–V polarization improved bending resistance at the expense of compressive strength (Figure 5C). These results indicate that radial and dorsoventral asymmetries can be leveraged as distinct yet complementary strategies for mechanical tuning. This radial shift—from a medulla-centered to cortex-dominant structure—not only increases *I* but also enhances stiffness routing, strain confinement, and directional resilience through internal symmetry modulation.

These computational findings are supported by our previous developmental study of frizzling chicken feathers [26], where we showed that the medulla, although mechanically soft, is crucial during rachis formation. In that work, defective integration between the ventral medulla and cortex disrupted dorsoventral patterning, resulting in incomplete ventral cortex development and a mechanically compromised shaft. This biological scenario demonstrates how internal material asymmetry—if mis-regulated—can lead to global structural failure. Here, by extending that insight into a mechanical modeling framework, we show that both internal (radial) and external (D–V) keratin allocations are central to how feather shafts achieve mechanical resilience through multiscale symmetry modulation.

Although our FEM models were simplified, their predictions are consistent with real feather shaft mechanics. In complementary compression tests on chicken and duck flight feathers, we observed dorsoventral differences in stiffness that parallel our simulations. The duck, which exhibits stronger D–V cortex polarization, showed significantly higher compressive stiffness in the dorsal and ventral cortex compared to the lateral regions. In contrast, the chicken—whose rachis morphology is more laterally reinforced—displayed a more uniform stiffness profile. While medullary structure and curvature may also influence these patterns, the alignment between empirical and modeled trends reinforces the importance of spatial keratin allocation in governing real-world mechanical anisotropy.

Taken together, this study bridges biological form, mechanical function, and design abstraction. By showing how directional keratin allocation governs performance in a geometrically constrained model, we highlight a fundamental principle: it is not just the material itself but its spatial deployment that enable resilience in lightweight biological beams.

Symmetry 2025, 17, 880 15 of 17

This strategy—mirroring the keratin polarization observed in feather rachises—suggests broader implications for structural design. Asymmetric reinforcement targeted toward zones of directional loading can enhance yield resistance and strain moderation without adding bulk. Such principles could be translated into engineered systems where localized reinforcement and energy dissipation are critical, such as bioinspired actuators, fatigue-resistant aerospace components, or morphing shell structures. In resource- or mass-constrained environments, like deployable shelters or planetary habitats, this geometry-driven material deployment—using a single material with spatially varied thickness—could offer modular, resilient performance without added complexity or diverse materials.

To contextualize our findings and guide future research, we acknowledge several limitations in the present study, particularly regarding model simplifications and biological generalizations.

While our FEM models captured macrostructural effects of cortex asymmetry, several technical limitations remain. For example, integrating real medullary porosity or laminar microstructures would require significantly finer meshing, leading to greater computational demand without proportionate gain in interpretability. Additionally, modeling dynamic or fatigue loading over flapping cycles would necessitate time-dependent boundary conditions and constitutive models that are beyond the scope of the current framework. Nevertheless, our simplified approach offers valuable insights into how geometric polarization influences bending resistance. We anticipate that future work incorporating realistic morphotypes and multiscale heterogeneity will refine these insights under more biologically complex scenarios.

Keratin is a hierarchically structured material, with regional variation in fibril alignment, density, and composition [6]. While our FEM models assumed homogeneous, bilinear elastic–plastic properties to isolate geometric effects, real feather rachises may exhibit localized material heterogeneity—especially at dorsal and ventral contact zones. Such internal heterogeneity, including porosity, lamination, and differential cross-linking, likely contributes to strain modulation and yield behavior. We acknowledge this limitation in our current modeling framework and suggest that future simulations incorporate position-dependent material properties derived from imaging or microscale testing to better capture the full spectrum of keratin's mechanical sophistication.

While this study focuses on dorsoventral (D–V) polarization, feather rachises exhibit asymmetries across multiple axes and scales. Beyond D–V distribution, features such as proximal–distal shaft tapering, dorsal ridges, and ventral invaginations can introduce localized reinforcements that further tailor mechanical performance. Although our FEM models abstracted these complexities to isolate D–V effects, such multiaxial asymmetries represent important directions for our future research. These higher-order geometric features may contribute to load redirection, strain redistribution, or torsional resistance, allowing for feather shafts to adapt to diverse flight regimes.

5. Conclusions

This study demonstrates how spatial variation in cortical keratin distribution—particularly along the dorsoventral axis—governs the mechanical behavior of hollow biological beam structures. Through finite element modeling with geometry-controlled conditions, we show that even modest asymmetries in material placement can substantially influence stiffness, strain localization, failure onset, and post-yield recovery. Dorsal reinforcement improves load tolerance by delaying strain localization and promoting elastic response, while ventral bias leads to premature plastic deformation and instability, despite identical global shape and material volume.

Symmetry 2025, 17, 880 16 of 17

Building upon previous developmental observations of rachis formation [26] and reinforcing them through newly acquired compression data, this work bridges morphological asymmetry and mechanical function. The alignment between simulation outcomes and real-tissue behavior strengthens the view that directional keratin allocation serves as a functional design strategy. Overall, our findings highlight spatial material organization—not compositional diversity—as a decisive principle underlying the structural performance of lightweight biological shafts.

Author Contributions: Conceptualization, H.W., J.-C.H. and W.-T.J.; Formal analysis, J.-C.H., W.-C.L. and Y.-S.W.; Investigation, H.W., J.-C.H. and W.-T.J.; Methodology, H.W., J.-C.H. and W.-T.J.; Project administration, W.-T.J.; Software, H.W. and J.-C.H.; Supervision, W.-T.J.; Visualization, H.W., J.-C.H., W.-C.L., X.-N.X. and W.-T.J.; Writing—original draft, H.W. and X.-N.X.; Writing—review and editing, H.W. and W.-T.J. All authors have read and agreed to the published version of the manuscript.

Funding: This work was supported by the National Science and Technology Council, Taiwan (MOST 111-2811-B-039-002, NSTC 112-2112-M-039-001, and NSTC 113-2112-M-039-001), China Medical University, Taiwan (CMU111-MF-18 and CMU113-MF-02).

Institutional Review Board Statement: The Institutional Animal Care and Use Committee (IACUC) of China Medical University reviewed and approved the animal use protocol.

Data Availability Statement: The authors confirm that the data supporting the findings of this study are available within the article.

Acknowledgments: The authors would like to thank colleagues and collaborators for their fruitful discussions and services provided by the Two-photon imaging facility at China Medical University Hospital, Taiwan.

Conflicts of Interest: The authors declare no conflicts of interest.

References

- 1. Wegst, U.G.; Bai, H.; Saiz, E.; Tomsia, A.P.; Ritchie, R.O. Bioinspired structural materials. *Nat. Mater.* **2015**, *14*, 23–36. [CrossRef] [PubMed]
- 2. Buehler, M.J. Tu(r)ning weakness to strength. Nano Today 2010, 5, 379–383. [CrossRef]
- 3. Fratzl, P.; Weinkamer, R. Nature's hierarchical materials. Prog. Mater. Sci. 2007, 52, 1263–1334. [CrossRef]
- 4. Meyers, M.A.; Chen, P.-Y.; Lin, A.Y.-M.; Seki, Y. Biological materials: Structure and mechanical properties. *Prog. Mater. Sci.* **2008**, 53, 1–206. [CrossRef]
- 5. Lazarus, B.S.; Chadha, C.; Velasco-Hogan, A.; Barbosa, J.D.; Jasiuk, I.; Meyers, M.A. Engineering with keratin: A functional material and a source of bioinspiration. *iScience* **2021**, 24, 102798. [CrossRef]
- 6. Wang, B.; Yang, W.; McKittrick, J.; Meyers, M.A. Keratin: Structure, mechanical properties, occurrence in biological organisms, and efforts at bioinspiration. *Prog. Mater. Sci.* **2016**, *76*, 229–318. [CrossRef]
- 7. Rajabi, M.; Ali, A.; McConnell, M.; Cabral, J. Keratinous materials: Structures and functions in biomedical applications. *Mater. Sci. Eng. C* **2020**, *110*, 110612. [CrossRef]
- 8. Banasaz, S.; Ferraro, V. Keratin from animal by-products: Structure, characterization, extraction and application—A review. *Polymers* **2024**, *16*, 1999. [CrossRef]
- 9. Sukmawati, D.; Eryani, A.; Damayanti, L. Silver Sulfadiazine's Effect on Keratin-19 Expression as Stem Cell Marker in Burn Wound Healing. *Biomedicine* **2020**, *10*, 5–11. [CrossRef]
- 10. Lingham-Soliar, T. Feather structure, biomechanics and biomimetics: The incredible lightness of being. *J. Ornithol.* **2014**, *155*, 323–336. [CrossRef]
- 11. Laurent, C.M.; Palmer, C.; Boardman, R.P.; Dyke, G.; Cook, R.B. Nanomechanical properties of bird feather rachises: Exploring naturally occurring fibre reinforced laminar composites. *J. R. Soc. Interface* **2014**, *11*, 20140961. [CrossRef] [PubMed]
- 12. Sullivan, T.N.; Wang, B.; Espinosa, H.D.; Meyers, M.A. Extreme lightweight structures: Avian feathers and bones. *Mater. Today* **2017**, 20, 377–391. [CrossRef]
- 13. Chang, W.-L.; Wu, H.; Chiu, Y.-K.; Wang, S.; Jiang, T.-X.; Luo, Z.-L.; Lin, Y.-C.; Li, A.; Hsu, J.-T.; Huang, H.-L. The making of a flight feather: Bio-architectural principles and adaptation. *Cell* **2019**, 179, 1409–1423.e17. [CrossRef] [PubMed]

Symmetry 2025, 17, 880 17 of 17

14. Chuang, T.; Cheng, J.-W.; Chuong, C.-M.; Juan, W.-T. Autofluorescence microscopy as a non-invasive probe to characterize the complex mechanical properties of keratin-based integumentary organs: A feather paradigm. *Chin. J. Phys.* **2023**, *86*, 561–571. [CrossRef]

- 15. Lingham-Soliar, T. Microstructural tissue-engineering in the rachis and barbs of bird feathers. Sci. Rep. 2017, 7, 45162. [CrossRef]
- 16. Bachmann, T.; Emmerlich, J.; Baumgartner, W.; Schneider, J.M.; Wagner, H. Flexural stiffness of feather shafts: Geometry rules over material properties. *J. Exp. Biol.* **2012**, 215, 405–415. [CrossRef]
- 17. Ansari, A.I.; Sheikh, N.A.; Kumar, N. Computational and experimental assessment of peacock feather. *Int. J. Interact. Des. Manuf.* (*IJIDeM*) **2024**, *19*, 1737–1749. [CrossRef]
- 18. Wang, S.; Chang, W.-L.; Zhang, Q.; Ma, M.; Yang, F.; Zhuo, D.; Hans, H.I.-C.; Yang, R.; Wu, P.; Habib, M. Variations of Mesozoic feathers: Insights from the morphogenesis of extant feather rachises. *Evolution* **2020**, *74*, 2121–2133. [CrossRef]
- 19. Wang, B.; Meyers, M.A. Seagull feather shaft: Correlation between structure and mechanical response. *Acta Biomater.* **2017**, *48*, 270–288. [CrossRef]
- 20. Cai, S.; Han, B.; Xu, Y.; Guo, E.; Sun, B.; Zeng, Y.; Hou, H.; Wu, S. Anisotropic composition and mechanical behavior of a natural thin-walled composite: Eagle feather shaft. *Polymers* **2022**, *14*, 309. [CrossRef]
- 21. Lu, Y.; Chen, Z.; Guo, E.; Kong, X.; Kang, H.; Xu, Y.; Li, R.; Fan, G.; Wang, T. Micro hierarchical structure and mechanical property of Sparrow Hawk (*Accipiter nisus*) feather shaft. *Comput. Model. Eng. Sci.* **2021**, 127, 705–720.
- 22. Deng, K.; Kovalev, A.; Rajabi, H.; Schaber, C.; Dai, Z.; Gorb, S. The damping properties of the foam-filled shaft of primary feathers of the pigeon Columba livia. *Sci. Nat.* **2022**, *109*, 1. [CrossRef] [PubMed]
- 23. Wang, B.; Meyers, M.A. Light Like a Feather: A Fibrous Natural Composite with a Shape Changing from Round to Square. *Adv. Sci.* **2017**, *4*, 1600360. [CrossRef] [PubMed]
- 24. Wu, H.; Chiu, Y.-K.; Tsai, J.-C.; Chuong, C.-M.; Juan, W.-T. A quantitative image-based protocol for morphological characterization of cellular solids in feather shafts. *STAR Protoc.* **2021**, *2*, 100661. [CrossRef]
- 25. Chen, C.-K.; Juan, W.-T.; Liang, Y.-C.; Wu, P.; Chuong, C.-M. Making region-specific integumentary organs in birds: Evolution and modifications. *Curr. Opin. Genet. Dev.* **2021**, *69*, 103–111. [CrossRef]
- 26. Wu, H.; Chuang, T.-C.; Liao, W.-C.; Chi, K.-J.; Ng, C.-S.; Cheng, H.-C.; Juan, W.-T. Modification of Keratin Integrations and the Associated Morphogenesis in Frizzling Chicken Feathers. *Biology* **2024**, *13*, 464. [CrossRef]
- 27. Mu, B.; Hassan, F.; Yang, Y. Controlled assembly of secondary keratin structures for continuous and scalable production of tough fibers from chicken feathers. *Green Chem.* **2020**, 22, 1726–1734. [CrossRef]
- 28. Bonser, R. The mechanical performance of medullary foam from feathers. J. Mater. Sci. Lett. 2001, 20, 941–942. [CrossRef]

Disclaimer/Publisher's Note: The statements, opinions and data contained in all publications are solely those of the individual author(s) and contributor(s) and not of MDPI and/or the editor(s). MDPI and/or the editor(s) disclaim responsibility for any injury to people or property resulting from any ideas, methods, instructions or products referred to in the content.